

**National Research Program „Cyber-physical systems,
ontologies and biophotonics for safe&smart city and society
(SOPHIS)**

**Project no.4 „Development of technologies for
secure and reliable smart city”**

Scientific report

Period 1

1. EDI BIGDATA

Research goal: Video and other signal content analysis gathered from large number of signal sources distributed over a smart city for safety purposes.

Task for the period 1: Develop concept for large scale video and other signal analysis and processing. Prepare scientific environment including High Performance Computing resources for signal content analysis and experimentation.

1.1. Smart city autonomous monitoring concept

According to smart city monitoring concept the city is equipped and monitored using conventional video surveillance cameras. In addition some other sensors can be attached. During the project the video analysis is mainly going to be considered due to its rich information in comparison to other type of signals. Nevertheless other signals will be considered for processing if necessary. The video gathering concept can be seen in Figure 1.1.

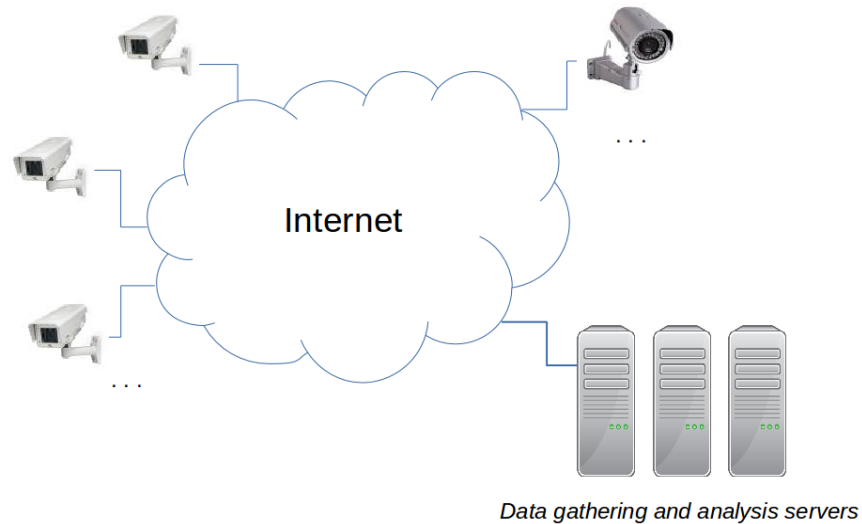


Fig. 1.1. Smart City video surveillance and safety monitoring system concept.

All data is gathered into special data storage and analysis servers. It is expected that monitoring and analysis system can run autonomously without human interaction. Only the analysis results can be accessed by authorized persons from the government.

The research scope of the BIGDATA group is focused on data processing methods and algorithms enabling signal content analysis. The main task for the group is to develop video processing methods which detect safety occasions and ignoration of regulations (for example: there is a car accident; car ignores the red light; a person ir carrying a gun etc.).

1.2. Deep Learning as the main research direction

Artificial neural networks under the name Deep Learning are recognized as a state-of-the-art in video analysis. It is promising and the most suited method for video and other signal content analysis. The considered smart city data processing will rely on

Deep Learning and further research will be mainly focused on comprehensive investigation of artificial neural networks.

Currently the Deep Learning approach is almost exclusively used into state-of-the-art image and speech recognition systems. The companies like Facebook, Google, Baidu are developing technologies based on artificial neural networks. For example, Facebook has developed the human face recognition system close to human abilities [1]. Similarly, all winners of image classification competition ILSVRC 2014 used Deep Learning in their submissions [2].

Evidently the learning of artificial neural networks is a recommended method for autonomous smart city monitoring and further efforts of BIGDATA group is going to be focused on a comprehensive investigation of Deep Learning.

1.3. Octave models for understanding Deep Learning

The Octave model of artificial neural networks has been created for better understanding its properties and behavior. Also it allows experimentally simulate various learning conditions and various network layer configurations.

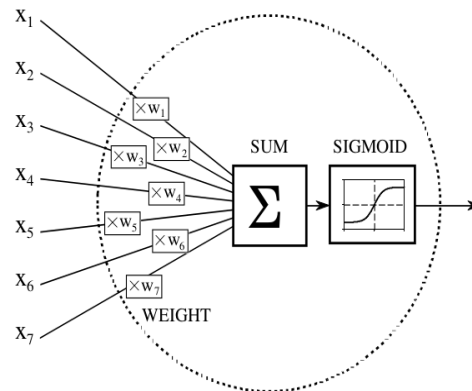


Fig. 1.2. Model of artificial neural network node [4].

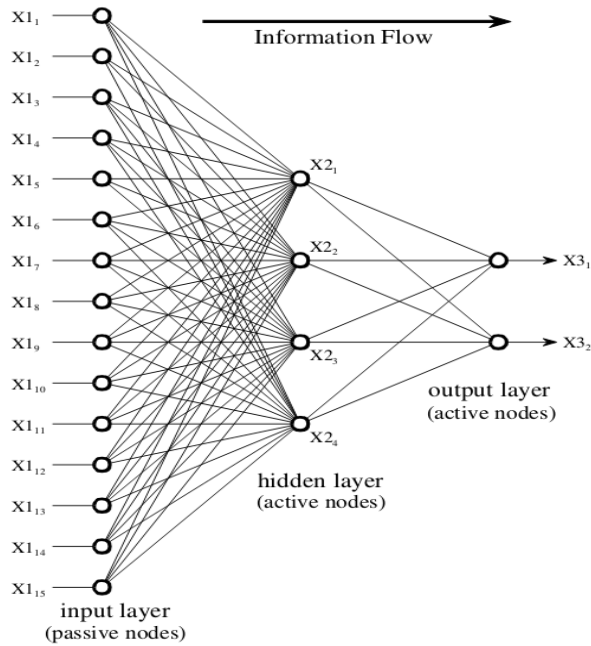


Fig. 1.3. Example of the artificial neural network [4].

In Figure 1.2 we can see a graphical representation of an artificial neural model which is the smallest entity in an artificial neural network. Structures of nodes organized in layers are making neural networks as it can be seen in Figure 1.3.

Using developed neural network models, all kind of learning and network architectures can be studied. Current attention is paid on fully connected and convolutional sigmoid neural network architectures together with back-propagation learning approach which is typical in image recognition. Also for this purpose the example of AlexNet is studied and described further in the report.

The Octave model is developed for relatively small data sets running on ordinary Personal Computers and it is not capable to process large quantity of images (millions) in reasonable time interval. For this purpose the High Performance Computing (HPC) is considered and the environment for relatively large scale network learning is prepared. The developed Octave models are well suited for fast validation of some network property relative to various artificial neural network architectures.

1.4. Preparation of EDI High Performance Computing environment

The framework for deep neural network learning has been prepared. It includes the EDI High Performance Computing server (2x Intel Xeon E5-2650v2 processors, 128 GB RAM, 2x480 GB SSD) configuration with 4 NVIDIA Tesla K20 graphic cards, installation of deep neural network configuration with learning software frameworks *Caffe* and *Torch7*. Usage of *Caffe* and *Torch7* is recognized as a good strategy for replacing CUDA lower-level graphic card programming.

The test deep network has been created according to AlexNet deep network configuration [3] and run on the EDI HPC server. For studying purposes, the detector “*Cat or rabbit*” has been developed based on the ImageNet labeled image data set. The detector “*Cat or rabbit*” can tell if the image contains a cat or a rabbit. The AlexNet neural network architecture can be seen in Figure 1.4.

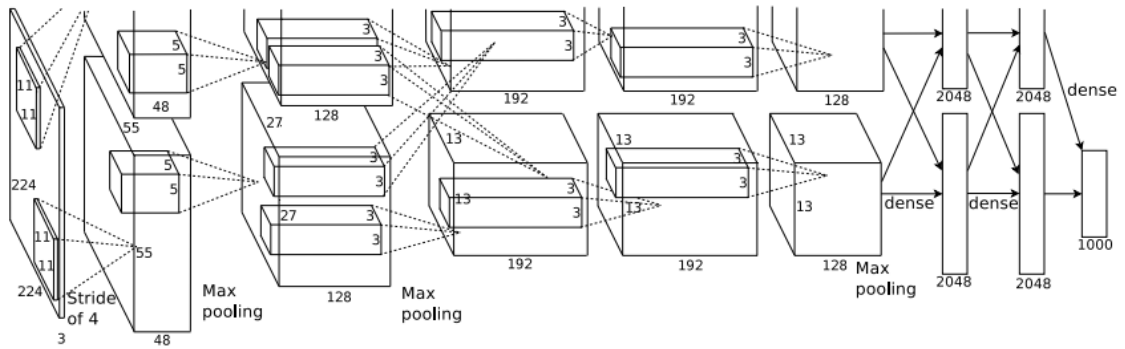


Fig. 1.4. Architecture of the AlexNet convolutional neural network used to implement “Cat or rabbit” image classifier for EDI HPC environment test purposes [3].

The neural network architecture shown in Figure 1.4 is implemented on EDI HPC server and it can be used for detection of various object classes. In smart city autonomous monitoring the object-in-time detection has to be considered because the object detection alone will not always provide necessary scene analysis. Perhaps the studied AlexNet deep network can be incorporated into the whole system. Also the performance issues have to taken into account.

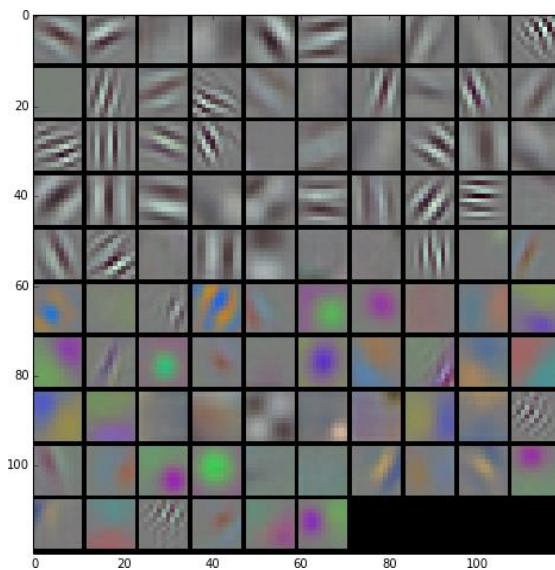


Fig. 1.5 Convolutional kernels of size $11 \times 11 \times 3$ learned by the first convolutional layer on the AlexNet [3].

In Figure 1.5 the first layer of learned AlexNet is shown. The picture is taken from publication [3]. First layers of deep neural networks are representation layers which consist of features needed for correct object detection in further neural network layers.

The size of a neural network in terms of each node weight coefficient count is directly related and defining the performance characteristics of the recognition system. Time needed for the analysis of image content should be small as possible. Therefore the size of neural networks should be as small as possible. This is

performance versus precision issue. For large image stream analysis the performance issues have to be taken into account.

Deep neural networks for object detection have been studied during the first project period, and the environment for deep learning has been prepared.

1.5. Implementation aspects of data gathering method using ASDM encoding

The specific data acquisition method was developed and the publication has been written describing it: K.Ozols, “Implementation of reception and real-time decoding of ASDM encoded and wirelessly transmitted signals”. The paper was presented at the IEEE Microwave and Radio Electronics Week 2015 in Pardubice, Czech Republic. The paper describes an implementation of reception and real-time decoding of signals encoded by the Asynchronous Sigma-Delta modulator (ASDM) and transmitted wirelessly on the basis of On-off keying. By using fast reconstruction algorithm if the signal length is 1 second, it is possible to reconstruct the original signal ≈ 25 times faster than by using classical reconstruction algorithm. If the length of the signal is 2, 4 and 8 seconds, the algorithm performs ≈ 61 , ≈ 130 and ≈ 228 times faster, respectively. Developed overall system consists of 3 parts: superheterodyne receiver, digitizer, and PC running adaptive data reconstruction algorithm. Real-time decoding algorithm, which consists of data acquisition, filtering, processing, reconstruction and visualization, is implemented in LabView as a virtual instrument with graphical user interface (GUI). The developed method can be considered in the context of data gathering approaches for smart city applications.

1.6. Further research and expected problems

Further work is considered to be focused on closer investigation of Deep Learning architectures and aspects of data gathering methods. For safety situation analysis the one of the main problems is unexistence of labeled learning data. It makes the problem of video content analysis especially difficult because one of crucial conditions for good usage of deep neural networks is availability of large labeled data sets for learning (some can be taken from the ImageNet project [2]). For further investigation the unlabeled data clustering based on deep neural networks is going to be considered (drawbacks may appear as a corruption of precision and situation recognition results) and other aspects of deep neural networks.

Summary

During the project period the following can be remarked:

1. Artificial neural networks under the name Deep Learning are recognized as a state-of-the-art. It is promising and the most suited method for video signal and other signal content analysis. The considered Smart City data processing will rely on Deep Learning and further experimentation will be mainly focused on comprehensive investigation of artificial neural networks.
2. The Octave model of artificial neural networks has been created for better understanding. It allows to experimentally simulate various learning conditions and various network layer configurations.
3. The framework for deep neural network learning has been prepared. It includes the EDI HPC server configuration with 4 NVIDIA Tesla K20 graphic cards and test example creation. For this purpose the detector “*Cat or rabbit*” has been developed based on ImageNet marked image data set [2]. The detector “*Cat or rabbit*” tells does the image consist cat or rabbit. The detector deep learning network configuration is from the AlexNet [3].

4. The data acquisition method was developed and the publication has been accepted K.Ozols, *Implementation of reception and real-time decoding of ASDM encoded and wirelessly transmitted signals*, IEEE MAREW 2015.

References

- [1] Yaniv Taigman, Ming Yang, Marc'Aurelio Ranzato, Lior Wolf, *DeepFace: Closing the Gap to Human-Level Performance in Face Verification*.
- [2] Internet: www.image-net.org/challenges/LSVRC/2014/
- [3] Alex Krizhevsky, Ilya Sutskever, Geoffrey E. Hinton, *ImageNet Classification with Deep Convolutional Neural Networks*.
- [4] Internet: www.dspguide.com

2. EDI REMSENS

During the reporting period multisensor data fusion possibilities were examined for the case when the data were obtained from sensors with different spatial resolution. Classifiers were developed to distinguish between land use categories, based on Bayesian classification principles. They were tested using the data published within the IEEE Geoscience and Remote Sensing section data fusion contest (DFC) (see http://cucciolo.dibe.unige.it/IPRS/IEEE_GRSS_IADFTC_2014_Data_Fusion_Contest.htm).

The task of the contest was to classify remote sensing images of land use categories, based on the RGB image from the RGB sensor (see Fig.2.1) and the TI image from the thermal sensor in the wavelength range from 7.8 μm to 11.5 μm (see Fig.2.2), both obtained during overflights of the same urban area.

Only "subset" images from one overflight of the RGB sensor and corresponding part of the TI image were processed, including all ground truth regions. Ground truth for the DFC was presented in a separate image with the same spatial resolution as the RGB image and covered ~17% of the whole area of the subset image. To prepare ground truth for the TI image, only pixels fully included in defined ground truth regions were used, comprising ~12% of the whole area of the subset TI image.

Our approach was to perform classification in two stages: in the first stage, two separate classifiers were designed, each using one of the available images only; in the second stage, these two classifiers were combined to increase the accuracy.



Fig. 2.1. City area RGB image with a pixel size of 20x20 cm. Ground truth data are marked for categories to be classified: road; trees, red roof; gray roof; concrete roof; vegetation; bare soil.

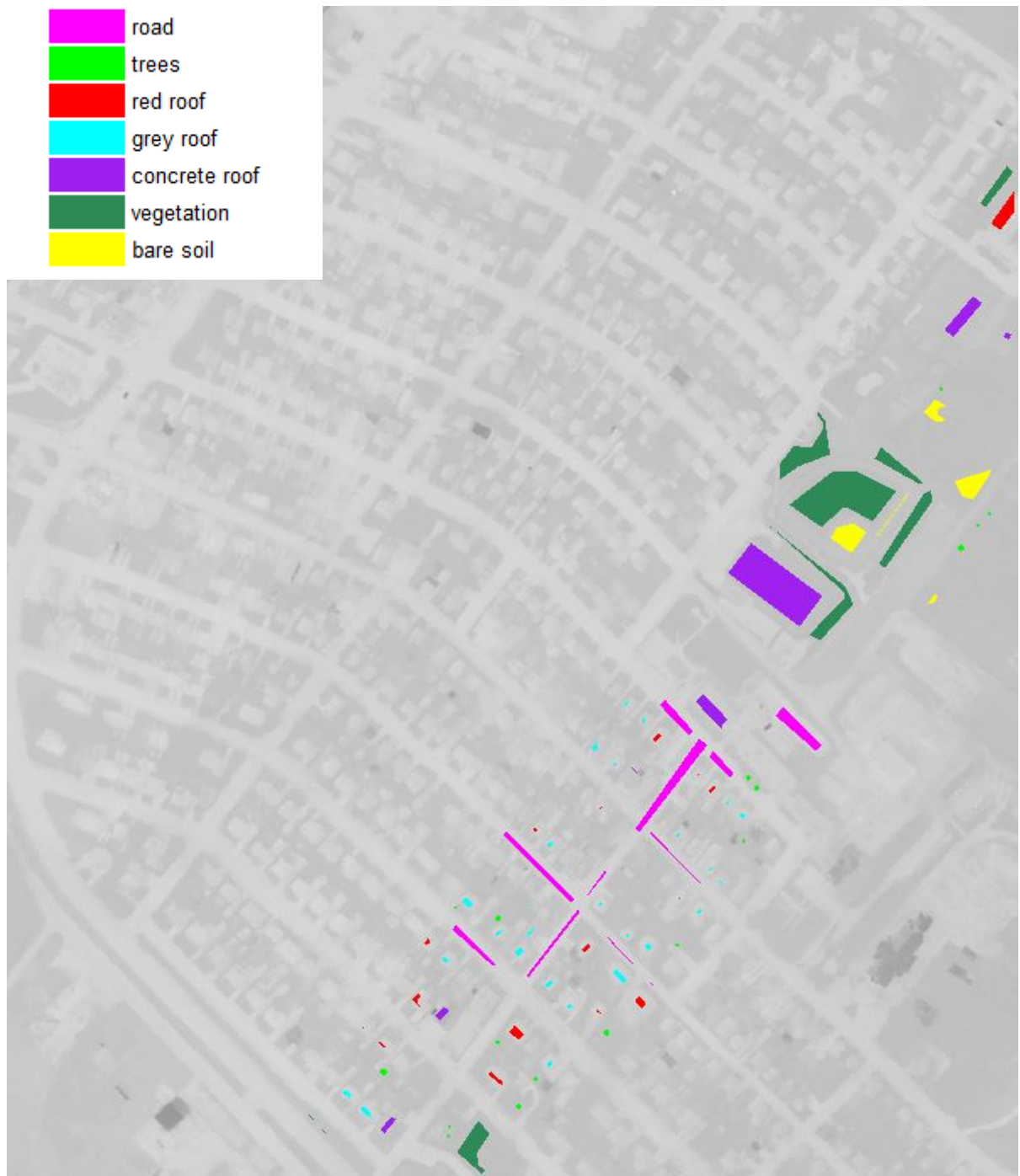


Fig.2.2. City area in one band of the thermal image with a pixel size of $\sim 1 \times 1$ m. Ground truth data are marked for categories to be classified.

Classifiers of land-use categories were developed on the basis of Bayesian classification principles using Gaussian, Dirichlet and gamma distributions for developing multi-dimensional data models. Classifiers were trained using available ground truth and checked for accuracy against pixels from the same area. RGB image with the best obtained classification results is shown in Fig.2.3.



Fig. 2.3. Processed RGB image with marked classified pixels (the best obtained classification results are shown).

Classification results of the single RGB image using multi-dimensional Gaussian distribution as the data model are presented in Table 2.1.

Table 2.1. Classification results of ground truth pixels, obtained by using Gaussian distribution model and exploiting data from RGB image only.

RGB		Obtained						
		Road	Trees	Red roof	Gray roof	Concrete roof	Vegetation	Bare soil
Analysed	Road	95,57%	0,00%	0,67%	2,91%	0,11%	0,01%	0,73%
	Trees	0,00%	90,03%	0,00%	0,01%	0,00%	9,96%	0,00%
	Red roof	0,32%	0,00%	95,70%	0,42%	0,04%	0,00%	3,50%
	Gray roof	9,81%	0,00%	1,24%	83,23%	5,24%	0,00%	0,48%
	Concrete roof	0,30%	0,00%	0,00%	2,80%	96,83%	0,00%	0,07%
	Vegetation	0,00%	6,36%	0,29%	0,28%	0,00%	91,07%	2,00%
	Bare soil	0,00%	0,11%	2,70%	0,30%	0,28%	2,27%	94,35%
Overall accuracy							93,03%	

It shows that the classifier is generally working well; major errors occur in the classification of gray roof pixels, which are misclassified as road. Tree pixels are partly taken as vegetation and vice versa. Such errors were expected because the mentioned pairs of categories are similar.

Single TI image classification results where the data model was based on multidimensional Gaussian distribution are shown in Table 2.2. It can be seen that this image alone can not be used for classification; concrete roofs in this spectral range can not be distinguished from trees and vegetation.

Table 2.2. Classification results of ground truth pixels, obtained by using Gaussian distribution model and exploiting data from TI image only.

TI		Obtained						
		Road	Trees	Red roof	Gray roof	Concrete roof	Vegetation	Bare soil
Analysed	Road	92,42%	0,01%	3,11%	3,55%	0,85%	0,00%	0,05%
	Trees	0,10%	38,40%	0,82%	0,78%	9,44%	42,48%	7,98%
	Red roof	5,04%	3,86%	47,76%	35,69%	3,52%	3,56%	0,58%
	Gray roof	4,92%	0,72%	34,69%	56,59%	2,82%	0,20%	0,06%
	Concrete roof	1,62%	30,73%	4,97%	6,40%	18,57%	29,06%	8,66%
	Vegetation	0,06%	27,39%	0,14%	0,19%	6,87%	57,08%	8,27%
	Bare soil	0,00%	13,75%	0,00%	0,00%	3,87%	28,40%	53,98%
Overall accuracy							54,88%	

Combined classification that uses both images (see. Table 2.3) allows to get better results than the individual image classifiers. It can be seen that the problems with gray roof pixels taken for road are largely resolved on the basis of TI image data.

Table 2.3. Classification results of ground truth pixels, obtained by using Gaussian distribution model and exploiting data from both images.

RGB+TI		Obtained						
		Road	Trees	Red roof	Gray roof	Concrete roof	Vegetation	Bare soil
Analysed	Road	96,27%	0,01%	1,07%	2,56%	0,09%	0,00%	0,00%
	Trees	0,00%	89,26%	0,00%	0,00%	0,00%	10,74%	0,00%
	Red roof	0,03%	0,00%	98,93%	0,89%	0,03%	0,00%	0,11%
	Gray roof	2,76%	0,00%	1,64%	91,12%	4,48%	0,00%	0,00%
	Concrete roof	0,16%	0,00%	0,20%	2,38%	97,23%	0,00%	0,03%
	Vegetation	0,00%	5,59%	0,24%	0,15%	0,00%	93,22%	0,80%
	Bare soil	0,00%	0,09%	0,33%	0,00%	0,31%	2,71%	96,55%
Overall accuracy							94,96%	

By checking use of the other distributions in the data model, it was concluded that the Gaussian distribution is the most appropriate. Tables 2.4 - 2.6 reflect the results obtained using Dirichlet multidimensional distribution but tables 2.7 - 2.9 correspond to the case when the gamma distribution is used. It can be seen that the results are worse than in the Gaussian distribution case. In addition, it is seen that classification of the TI image using the gamma distribution is so bad, that combination of images does not improve, but even worsen the classification done from RGB image alone.

The idea was put forward that it might be appropriate to use different probability distributions for processing of RGB and TI images. However the most accurate combined classifier was obtained when the Gaussian model was used for both images.

During studies of application of different distributions, an approach for combining distributions in a data model was developed, and it turned out that such approach is productive. Classification results obtained by using a classifier constructed on the basis of combination of Gaussian and Dirichlet distributions in a data model are shown in Table 2.10. Similarly, results obtained by combination of Gaussian and gamma distributions in a data model are shown in Table 2.11, for combination of Dirichlet and gamma distributions in a data model in Table 2.12. And finally, all 3 analyzed distributions were combined in a data model and corresponding results are shown in Table 2.13. It can be seen that the best results are obtained in the latter case. We can put forward the hypothesis that combination of distributions improves the model so that such combination can be used intentionally to improve classification results. It will be further investigated during the next project periods.

Table 2.4. Classification results of ground truth pixels, obtained by using Dirichlet distribution model and exploiting data from RGB image only.

RGB		Obtained						
		Road	Trees	Red roof	Gray roof	Concrete roof	Vegetation	Bare soil
Analysed	Road	92,44%	0,00%	1,19%	5,48%	0,25%	0,08%	0,55%
	Trees	0,01%	75,90%	0,01%	0,33%	0,08%	23,67%	0,00%
	Red roof	0,27%	0,00%	93,33%	1,60%	0,06%	0,03%	4,71%
	Gray roof	6,01%	0,00%	2,40%	87,16%	4,40%	0,02%	0,00%
	Concrete roof	0,73%	0,00%	0,28%	2,32%	96,63%	0,04%	0,00%
	Vegetation	0,03%	3,90%	0,55%	0,06%	0,18%	88,66%	6,62%
	Bare soil	0,00%	0,10%	10,01%	0,00%	0,25%	1,75%	87,89%
Overall accuracy							90,65%	

Table 2.5. Classification results of ground truth pixels, obtained by using Dirichlet distribution model and exploiting data from TI image only.

TI		Obtained						
		Road	Trees	Red roof	Gray roof	Concrete roof	Vegetation	Bare soil
Analysed	Road	62,87%	0,16%	5,98%	8,77%	4,32%	0,22%	17,69%
	Trees	2,79%	23,15%	5,83%	6,84%	19,33%	35,55%	6,51%
	Red roof	6,40%	5,54%	41,58%	33,48%	4,71%	6,55%	1,74%
	Gray roof	8,15%	5,01%	36,41%	40,14%	5,13%	3,39%	1,76%
	Concrete roof	5,31%	18,78%	10,60%	5,84%	30,15%	20,64%	8,68%
	Vegetation	1,19%	21,46%	3,90%	3,96%	16,27%	44,12%	9,10%
	Bare soil	1,74%	15,57%	4,54%	2,98%	13,94%	13,33%	47,90%
Overall accuracy							44,16%	

Table 2.6. Classification results of ground truth pixels, obtained by using Dirichlet distribution model and exploiting data from both images.

RGB+TI		Obtained						
		Road	Trees	Red roof	Gray roof	Concrete roof	Vegetation	Bare soil
Analysed	Road	93,44%	0,00%	0,90%	4,58%	0,22%	0,08%	0,78%
	Trees	0,01%	76,48%	0,03%	0,36%	0,08%	23,03%	0,01%
	Red roof	0,09%	0,00%	95,54%	1,58%	0,02%	0,51%	2,26%
	Gray roof	1,31%	0,00%	2,20%	92,97%	3,39%	0,14%	0,00%
	Concrete roof	0,61%	0,00%	0,04%	2,24%	95,14%	0,67%	1,31%
	Vegetation	0,02%	4,78%	2,00%	0,05%	0,18%	90,92%	2,05%
	Bare soil	0,00%	0,09%	18,44%	0,00%	0,10%	9,12%	72,24%
Overall accuracy							90,70%	

Table 2.7. Classification results of ground truth pixels, obtained by using gamma distribution model and exploiting data from RGB image only.

RGB		Obtained						
		Road	Trees	Red roof	Gray roof	Concrete roof	Vegetation	Bare soil
Analysed	Road	57,25%	0,00%	0,00%	0,00%	0,53%	3,00%	39,22%
	Trees	0,13%	17,94%	0,00%	0,00%	0,00%	80,89%	1,03%
	Red roof	21,13%	0,02%	0,00%	0,00%	0,18%	51,74%	26,93%
	Gray roof	22,35%	0,26%	0,00%	0,00%	11,50%	53,59%	12,31%
	Concrete roof	0,11%	0,01%	0,00%	0,00%	99,35%	0,03%	0,49%
	Vegetation	4,60%	0,32%	0,00%	0,00%	0,00%	93,02%	2,06%
	Bare soil	3,90%	0,00%	0,00%	0,00%	1,18%	1,95%	92,98%
Overall accuracy							71,64%	

Table 2.8. Classification results of ground truth pixels, obtained by using gamma distribution model and exploiting data from TI image only.

TI		Obtained						
		Road	Trees	Red roof	Gray roof	Concrete roof	Vegetation	Bare soil
Analysed	Road	96,41%	0,38%	0,00%	3,09%	0,00%	0,00%	0,11%
	Trees	0,42%	10,11%	0,00%	1,69%	0,00%	6,98%	80,80%
	Red roof	78,08%	3,72%	0,00%	10,92%	0,00%	0,34%	6,95%
	Gray roof	78,46%	3,38%	0,00%	17,41%	0,07%	0,00%	0,69%
	Concrete roof	11,36%	10,68%	0,00%	1,45%	1,47%	4,04%	70,99%
	Vegetation	0,14%	10,64%	0,00%	0,16%	0,00%	13,06%	76,00%
	Bare soil	0,00%	0,45%	0,00%	0,00%	0,00%	4,16%	95,39%
Overall accuracy							32,88%	

Table 2.9. Classification results of ground truth pixels, obtained by using gamma distribution model and exploiting data from both images.

RGB+TI		Obtained						
		Road	Trees	Red roof	Gray roof	Concrete roof	Vegetation	Bare soil
Analysed	Road	98,44%	0,16%	0,00%	1,04%	0,05%	0,00%	0,31%
	Trees	0,62%	15,04%	0,00%	1,27%	0,00%	81,25%	1,82%
	Red roof	82,02%	2,16%	0,02%	6,94%	0,00%	1,56%	7,30%
	Gray roof	80,02%	2,12%	0,00%	12,09%	4,31%	0,59%	0,86%
	Concrete roof	9,99%	0,03%	0,00%	0,07%	31,79%	0,00%	58,12%
	Vegetation	0,15%	1,26%	0,00%	0,10%	0,00%	90,42%	8,06%
	Bare soil	0,00%	0,00%	0,00%	0,00%	0,00%	1,39%	98,60%
Overall accuracy							66,81%	

Table 2.10. Classification results of ground truth pixels, obtained by using data model combined from Gaussian and Dirichlet distributions and exploiting data from both images.

RGB+TI		Obtained						
		Road	Trees	Red roof	Gray roof	Concrete roof	Vegetation	Bare soil
Analysed	Road	95,52%	0,00%	1,44%	2,93%	0,10%	0,00%	0,00%
	Trees	0,00%	82,89%	0,03%	0,08%	0,00%	16,99%	0,00%
	Red roof	0,01%	0,00%	98,02%	1,22%	0,03%	0,00%	0,72%
	Gray roof	0,65%	0,00%	1,78%	93,54%	4,02%	0,00%	0,00%
	Concrete roof	0,24%	0,00%	0,10%	2,56%	96,94%	0,00%	0,15%
	Vegetation	0,00%	3,35%	0,36%	0,08%	0,00%	95,24%	0,97%
	Bare soil	0,00%	0,09%	1,39%	0,00%	0,23%	3,59%	94,70%
Overall accuracy							95,23%	

Table 2.11. Classification results of ground truth pixels, obtained by using data model combined from Gaussian and gamma distributions and exploiting data from both images.

RGB+TI		Obtained						
		Road	Trees	Red roof	Gray roof	Concrete roof	Vegetation	Bare soil
Analysed	Road	97,85%	0,01%	0,66%	1,26%	0,09%	0,00%	0,13%
	Trees	0,00%	79,35%	0,00%	0,32%	0,00%	20,33%	0,00%
	Red roof	1,47%	0,00%	85,89%	5,35%	0,03%	0,25%	6,99%
	Gray roof	18,58%	0,02%	0,77%	75,24%	5,16%	0,00%	0,23%
	Concrete roof	0,38%	0,00%	0,08%	1,43%	97,97%	0,00%	0,14%
	Vegetation	0,00%	2,23%	0,05%	0,21%	0,00%	96,16%	1,35%
	Bare soil	0,00%	0,03%	0,00%	0,00%	0,30%	2,21%	97,46%
Overall accuracy							94,14%	

Table 2.12. Classification results of ground truth pixels, obtained by using data model combined from Dirichlet and gamma distributions and exploiting data from both images.

RGB+TI		Obtained						
		Road	Trees	Red roof	Gray roof	Concrete roof	Vegetation	Bare soil
Analysed	Road	97,63%	0,00%	1,33%	0,77%	0,11%	0,15%	0,01%
	Trees	0,00%	70,08%	0,31%	0,01%	0,00%	29,60%	0,00%
	Red roof	0,46%	0,00%	88,63%	2,25%	0,02%	2,29%	6,35%
	Gray roof	7,54%	0,00%	1,38%	86,16%	4,28%	0,64%	0,00%
	Concrete roof	0,86%	0,00%	0,04%	1,10%	96,61%	0,43%	0,95%
	Vegetation	0,00%	0,62%	0,22%	0,01%	0,00%	96,75%	2,40%
	Bare soil	0,00%	0,01%	0,00%	0,00%	0,08%	4,41%	95,51%
Overall accuracy							94,56%	

Table 2.13. Classification results of ground truth pixels, obtained by using data model combined from Gaussian, Dirichlet and gamma distributions and exploiting data from both images.

RGB+TI		Obtained						
		Road	Trees	Red roof	Gray roof	Concrete roof	Vegetation	Bare soil
Analysed	Road	97,45%	0,00%	1,26%	1,18%	0,10%	0,00%	0,00%
	Trees	0,00%	78,94%	0,00%	0,03%	0,00%	21,03%	0,00%
	Red roof	0,23%	0,00%	91,94%	2,03%	0,03%	0,30%	5,47%
	Gray roof	3,25%	0,00%	1,18%	91,18%	4,40%	0,00%	0,00%
	Concrete roof	0,40%	0,00%	0,07%	1,94%	97,38%	0,00%	0,20%
	Vegetation	0,00%	1,38%	0,16%	0,08%	0,00%	97,08%	1,29%
	Bare soil	0,00%	0,05%	0,00%	0,00%	0,23%	2,87%	96,85%
Overall accuracy							95,79%	

Described results were prepared for presentation in the conference „Electronics 2015”.

3. EDI RADAR

3.1. Short range UWB radar sensor applications for room security systems

UWB radar sensor working principle

The radar sensor principle - sounding a scenario under test using radio waves in the GHz range and process the obtained echo signal.

The radar echo depends on target size, shape and material composition and also from the test room configuration. The desired information: distance, location, orientation, speed, shape, material composition.

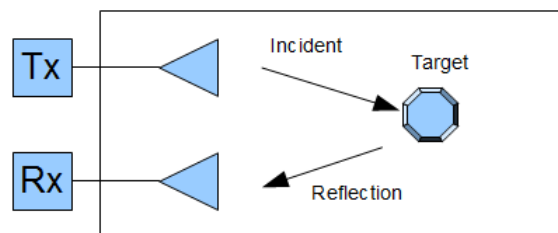


Fig. 3.1. Fundamental impulse radar principle

Short Range Devices using UWB technology standardisation in Europe

The short range device using UWB technology standardisation work in Europe is carried out by the European Telecommunications Standards Institute (ETSI). ETSI's

standardization activity for short-range devices currently includes the following UWB applications [1]:

- Communications applications
- Ground-probing and wall-probing radar
- Tank level probing radar
- Sensors
- Precision location within buildings
- Automotive radar.

From the list of applications the following complies with the project tasks: 1) Ground-probing and wall-probing radar; 2) Sensors; 3) Precision location within buildings. So only these three groups of applications will be examined in more detail.

1. Ground-probing and wall-probing radar

The expected operating frequency range is from 30 MHz to 12.4 GHz, with a very high bandwidth and a very low radiated power density. More detailed information about this type of devices can be found in ETSI Technical report [2] and in the standard [3].

2. UWB sensor applications.

From the ETSI listed applications the following complies with the projects objectives:

- 2.1. Building Material Analysis and Classification equipment (2.2-8.5 GHz) [4]
- 2.2. Location tracking applications for person and object tracking and industrial applications (3,4 GHz-4,8 GHz) (6 GHz-8,5 GHz)

UWB radar sensor resolution [5]

- 1) Range resolution (δ_r) – the ability to of the radar sensor to distinguish between two closely located point targets of identical radar cross section

$$\delta_r \approx \frac{t_w c}{2} \approx \frac{c}{2BW} \quad (3.1)$$

- 2) Range accuracy (δ_A) – minimum range error for a single point target that can be attained in case of noise-affected measurements.

$$\delta_A = \frac{c\phi_j}{2} = \frac{ct_r}{2\sqrt{SNR}} \approx \frac{c}{4BW\sqrt{SNR}} \quad (3.2)$$

Experimental application tests

During the first project period experimental application tests were carried out to test the potential applications of the UWB radar sensor technology for security monitoring systems.

A quasi-monostatic radar configuration experimental UWB test setup (Fig. 3.2) was made for application testing purposes. The test setup consisted of two identical

¹Ultra Wide Band. (2015, October 4). Retrieved from <http://www.etsi.org/technologies-clusters/technologies/radio/ultra-wide-band?highlight=YToxOntpOjA7czo0OiJ1d2liO30=>

² Technical characteristics for SRD equipment using Ultra Wide Band technology (UWB); Part 2: Ground- and Wall- Probing Radar applications; System Reference Document: **ETSI TR 101 994-2**

³ Ground- and Wall- Probing Radar applications (GPR/WPR) imaging systems: **ETSI EN 302 066**

⁴ Building material analysis and classification applications operating in the frequency band from 2.2 GHz to 8 GHz. Technical report: **ETSI TR 102 495-1**; Standard: **ETSI EN 302 435**

⁵ SACHS, Jürgen. Handbook of Ultra-wideband Short-range Sensing: Theory, Sensors, Applications. John Wiley & Sons, 2013.

shielded and resistively loaded Bow-Tie (planar conical) type antennas, an avalanche transistor based impulse generator and a real-time 20 GHz bandwidth oscilloscope (Tektronix DPO72004C). The antennas were mounted on a test stand in the middle of the room to minimise the reflections from the ceiling, floor and the walls.

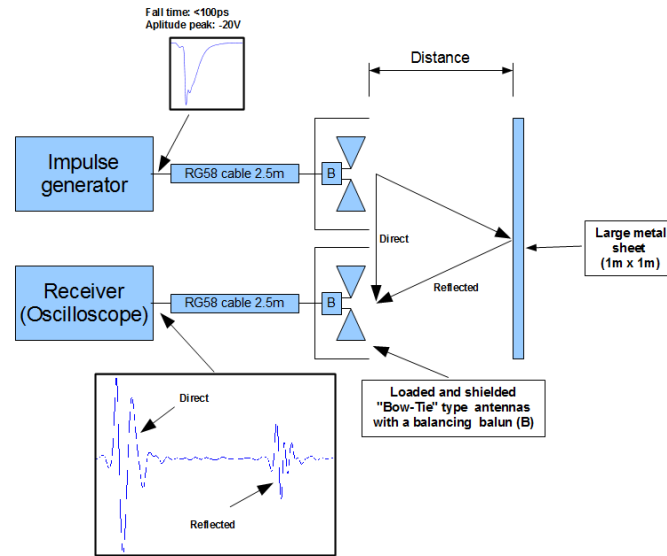


Fig. 3.1 Experimental test setup.

To measure the distance (x) to an object using a quasi-monostatic radar configuration the following, simplified formula could be used.

$$x = \frac{c}{2\sqrt{\epsilon_r}}(t_2 - t_1), \quad (3.3)$$

- Where x – distance (meters);
- c – Speed of light ($3 * 10^8$ m/s);
- ϵ_r – Relative permittivity of the of the medium;
- t_2 – Reflected impulse peak time moment;
- t_1 – Direct impulse peak time moment.

The simplified distance calculation formula is correct when the distance to an object is noticeably larger than the distance between the transmitting and receiving antennas.

An experimental test result from an object in 80cm distance from the antennas is shown in Fig. 3.1.

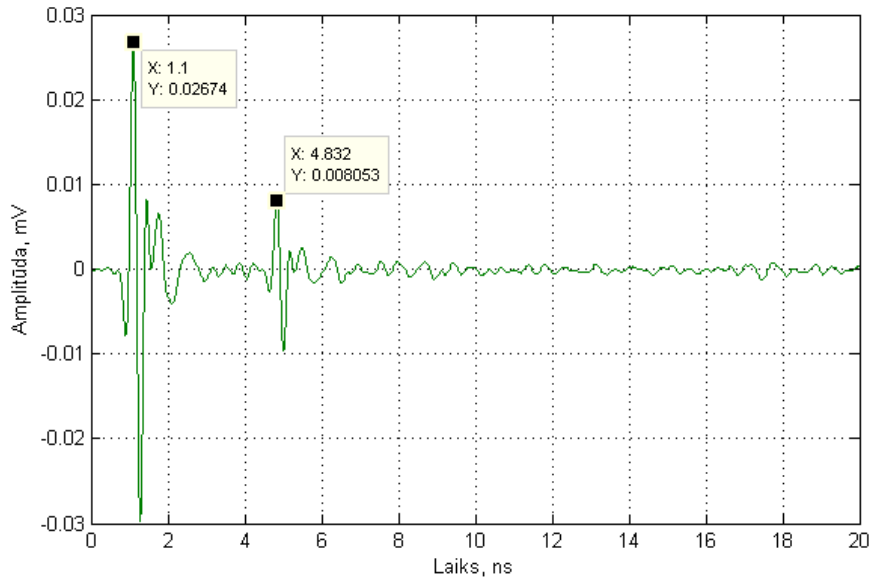


Fig. 3.2. Object in 80 cm distance from the antennas.

The response (reflection) from an object decreases by increasing the distance to the object, which can be seen in Fig. 3.3.

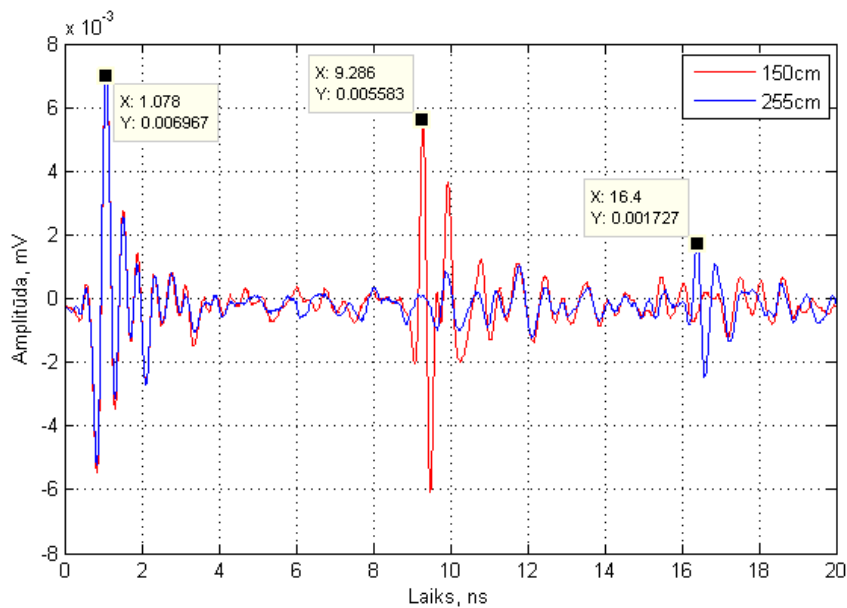


Fig. 3.3. Object in 150 cm and 255 cm distance from the antennas.

A set of distance measurements were performed and the results are summarised in Table 3.1.

Table 3.1. Distance measurement experiment results.

Real distance	From measurements	Difference
80cm	85.94cm	5.94cm
140cm	143.21cm	3.21cm
150cm	153.16cm	3.16cm
192cm	194.11cm	2.11cm
255cm	257.67cm	2.67cm

The UWB radar sensors can be also used to detect object behind other objects, what cannot be done using other optical or sound sensors. To demonstrate this idea a plywood sheet was placed in between the antennas and the metal sheet used in previously used experimental setup. The measurement (see Fig. 3.4) showed that the reflections from the plywood sheet and from the metal sheet can be clearly seen.

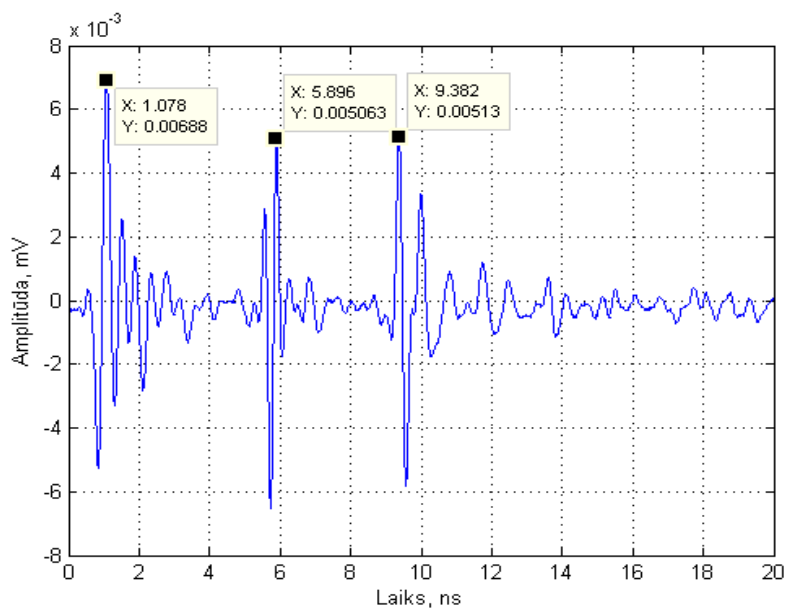


Fig. 3.4. Reflectogram from a metal sheet behind a plywood sheet.

The UWB radar sensor can be also used for non-metallic material thickness testing. For safety monitor applications remote ice thickness measurements could be useful. To test UWB radar sensor ice thickness measurement capabilities an indoor test setup was made (Fig. 3.5). For the measurements the same hardware was used as in previous tests, only the configuration was changed.

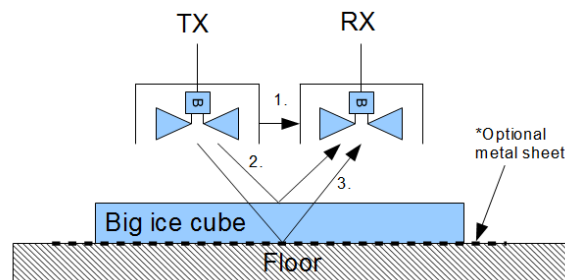


Fig. 3.5. Indoor ice thickness measurement test setup.

From the measurement test setup can be seen that the measurement signal should contain three components: 1. – the direct pulse; 2. – reflection from air/ice transition; 3. – reflection from ice/floor transition.

Experimental measurements using different thickness ice cubes were made. From the 5 cm and 17 cm thick ice cube measurements signals in Fig. 3.6 it can be seen, that: 1) the sounding impulse is too long to correctly measure ice thickness below 10cm; 2) the long antenna ringing makes the peak detection more difficult on larger ice thickness measurements.

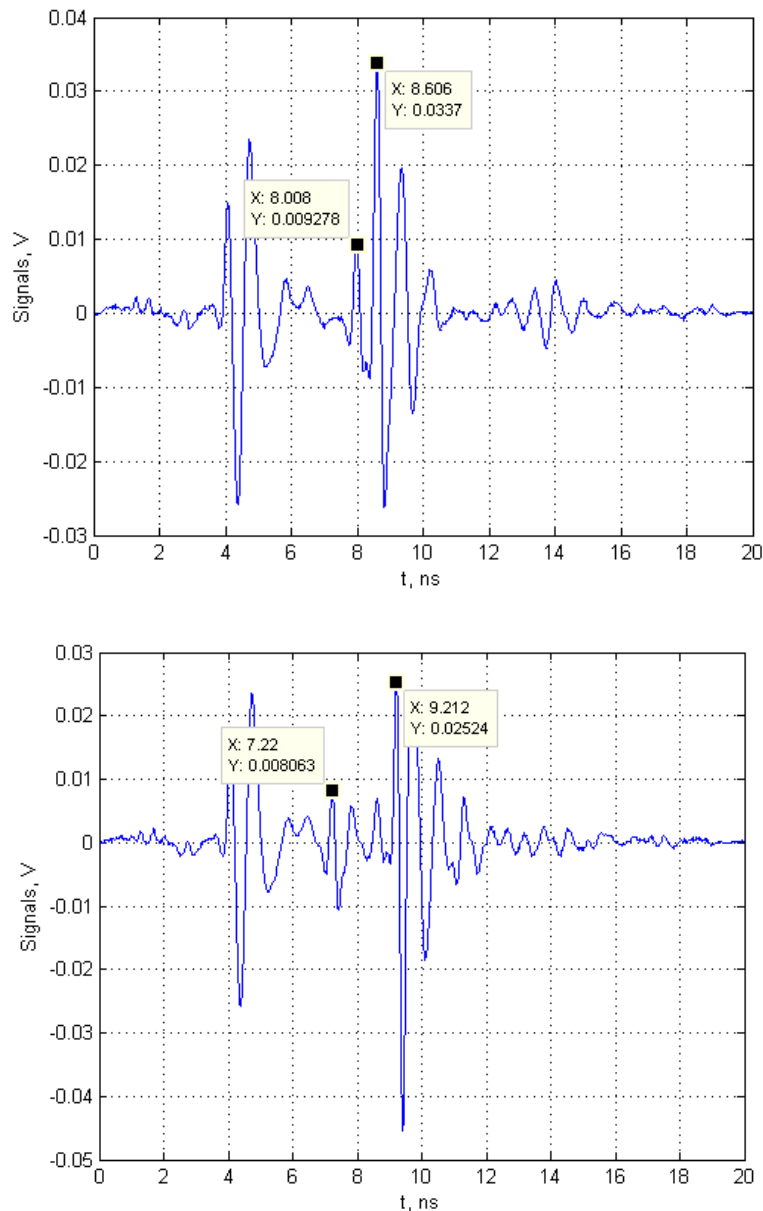


Fig. 3.6. Signals from a 5cm (upper) and 17cm (lower) thick ice cube.

After measuring the travel time (t) in the ice layer from the reflected impulse peaks and a-priori knowing the material dielectric constant (ϵ), the ice thickness could be

calculated using a simplified equation 3.4 [6].

$$x = \frac{c}{2 \cdot \sqrt{\epsilon}} \cdot t \quad (3.4)$$

The opposite calculation of the materials dielectric constant can be done by expressing the dielectric constant from the equation 3.4, the result is equation 3.5.

$$\epsilon = \left(\frac{c \cdot t}{2 \cdot x} \right)^2 \quad (3.5)$$

The results from three different ice block thickness measurements are summarised in Table 3.2.

Table 3.2. Ice thickness measurement results.

Ice thickness	Time between impulse peaks, ns	Calculated ϵ	Calculated ice thickness using $\epsilon = 3.1$	Error, %
5 cm	0.598	3.2184	5.095 cm	1.9
11 cm	1.286	3.0752	10.956 cm	0.4
17 cm	1.992	3.0893	16.971 cm	0.2

3.2. Research on signal processing methods for detection of changes in a room, object displacement detection.

A UWB radar sensor can be used for obtaining a room's impulse response [], which consists of reflections from the room walls and the objects inside the room. The object can be fixed, like a chair or a table, or can be moving. Small object movements can be masked by bigger reflections from larger non-moving objects. To detect small objects movements in the room, which are masked by reflections from other stationary objects in the room, signal processing should be applied.

A Research on applying the method of principal components analysis (PCA) for detection of small target movements in ultra-wideband radar sensor systems has been carried out.

The tested method of signal processing is based on the well-known Karhunen-Loeve transform (principal component analysis). Initial implementation of the signal, having a high redundancy of information, translated into the space of principal components. The signal on the first principal component is the basic information about the signal's changes caused by very small movements in the test area. The algorithm is described in detail in an earlier publication [7].

A test setup was made using an in-house made UWB pulse radar sensor, designed for remote human respiratory movement detection [8]. The test setup (Fig. 3.7) consists of

⁶ MEASUREMENT OF LAKE ICE THICKNESS WITH A SHORT-PULSE RADAR SYSTEM / Obtained from. - <http://ntrs.nasa.gov/archive/nasa/casi.ntrs.nasa.gov/19760013526.pdf>

⁷ M. Greitans and V. Aristov, "Conservation of the Law of Phase Modulation for UWB Pulse Signals in the First Principal Component", "Automatic Control and Computer Sciences" Vol.46, Number 4, 2012, Allerton Press, Inc. pp.179-184.

⁸ Vladimir Aristov, "UWB radar "sees" a human's breathing in the space of principal components", Applied Sciences in Europe: tendencies of contemporary development, 1st International Scientific conference, 21-22th March 2013, Stuttgart, Germany. (ISSN 2195-2183) lpp. 138-139.

an UWB radar sensor, fixed at an angle relative to the floor in which antenna systems field of view an object is been moved.

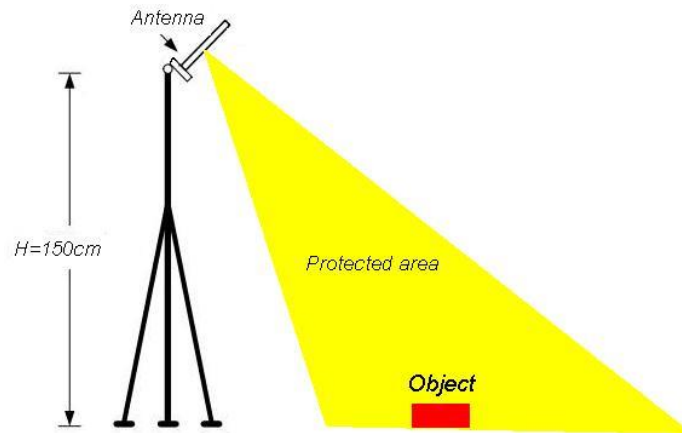


Fig. 3.7. Test setup.

Before the experimental tests, a system test measurement is made and a reflection from a 410×230 mm metal sheet is obtained (Fig. 3.8). The central frequency of the test reflected pulse is 3GHz and the (0.7 level) bandwidth is 1.3 GHz

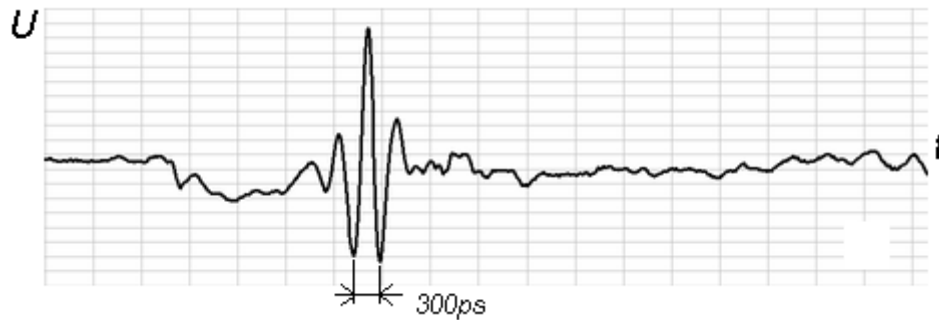


Fig. 3.8. Test reflection from a large metal sheet.

At first the method was tested on a set reflected signals when no object movement in the test area was performed (Fig. 3.9). The result is a noise-like signal.

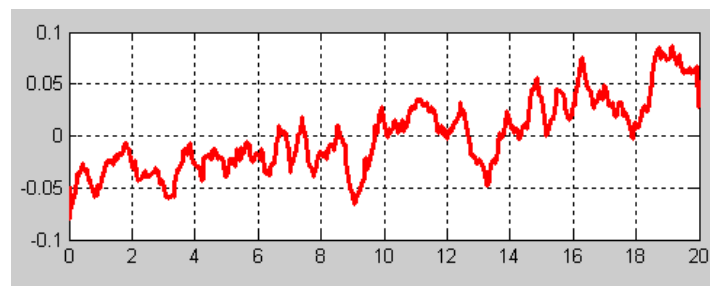


Fig. 3.9. No movement in the area (noise).

Applying the method on a set of reflected signals when a person walked slowly one time (left) and two time fast (right) through the test area results in a pulse-like signals that can be seen in Fig. 3.10.

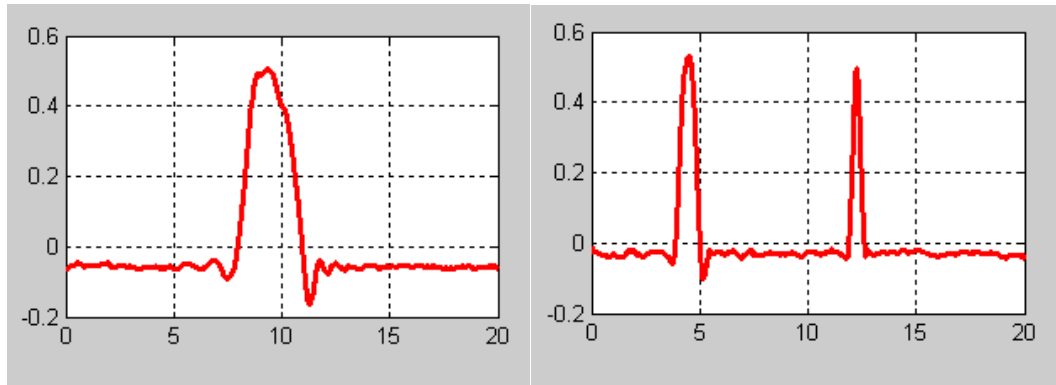


Fig. 3.10. Person walked slowly (left) and two times faster (right) through the test area.

3.3. Development of UWB radar sensor functional parts.

One of the main tasks for period 1 was to build a prototype of the UWB radar sensor. Sensor had to be able to work autonomously, make local computations if necessary and transmit data to other devices like smartphone, tablet or personal computer. Additionally a LCD display was included for debug and local data indication purposes. UWB radar sensor uses sampling receiver principles which samples received high frequency signal and converts it to low frequency equivalent time signal. That reduces requirements for PCB of the main sensor board other than receiver module.

Block diagram of UWB radar sensor is presented below.

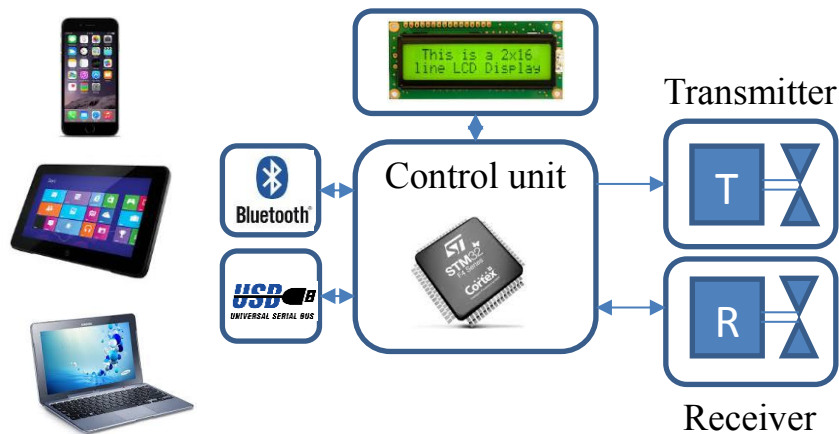


Fig. 3.11. Radar Sensor block diagram.

Important part of the equivalent time sampling receiver is the time scale circuit. To acquire stability and low jitter on sampled signal it is essential to build time scale circuit with low noise and distortions. In this prototype two saw shaped signals are used and compared to acquire equivalent time scale. Slow sloped saw-shaped signal is made by DAC since its only requirement is low noise. As for fast sloped saw signal it is important to have linear slope and low noise on a 10 to 25 ns slope. Circuit that generates fast slope saw-shape signal is illustrated in Fig. 3.13.

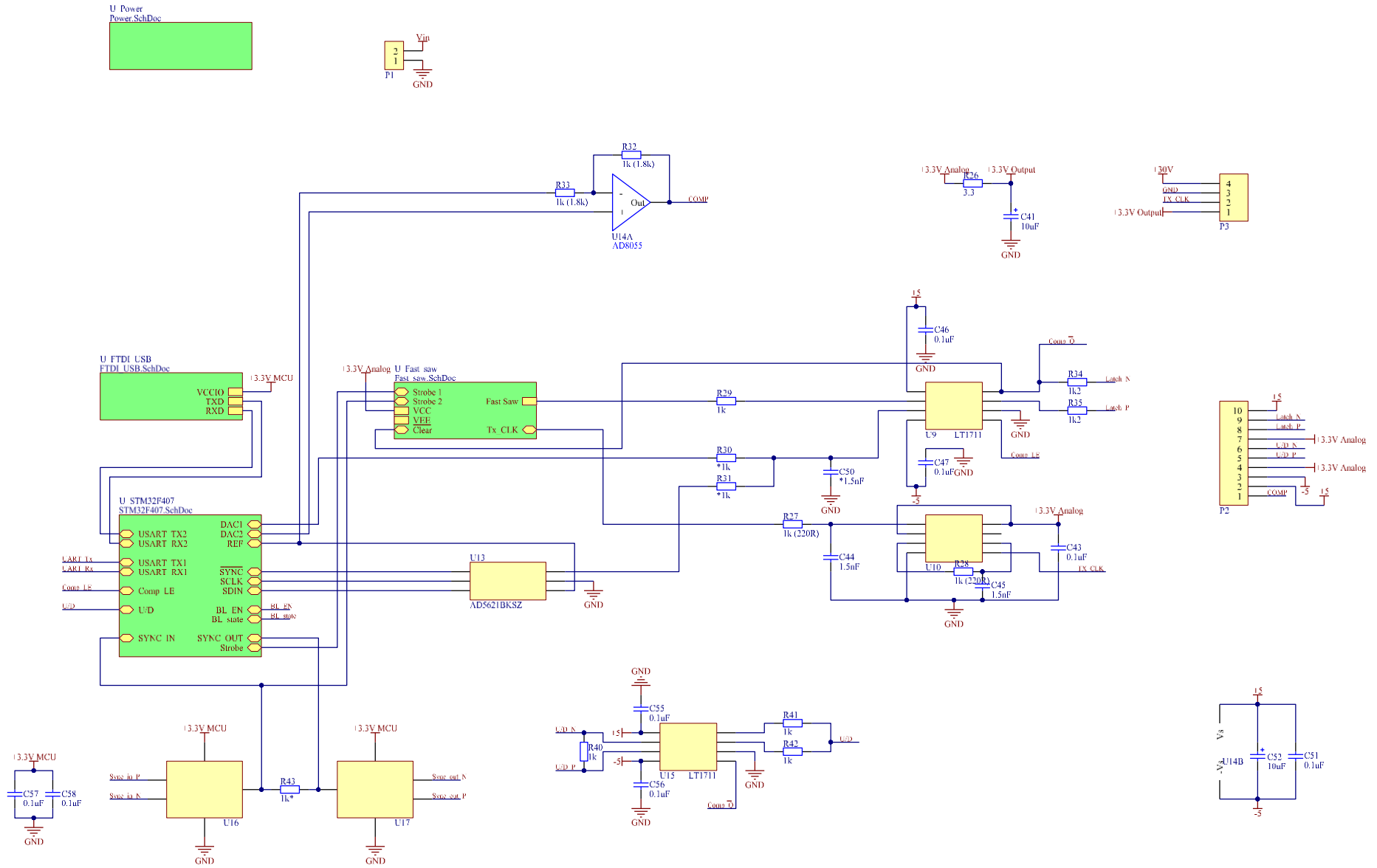


Fig. 3.12. Complete UWB radar sensor circuit.

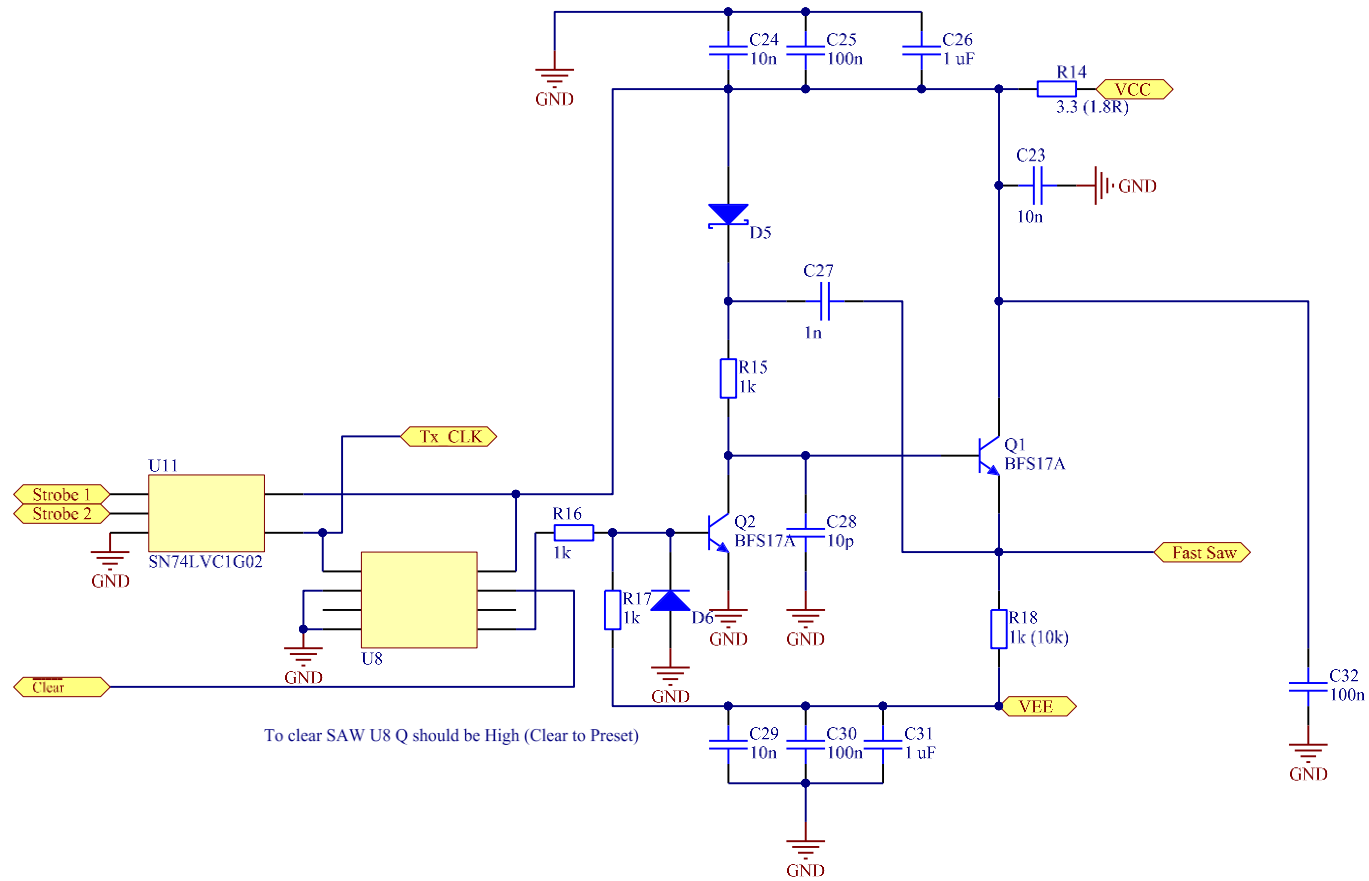


Fig. 3.13. Fast slope saw-shape generator.

In addition to MCU and timing circuit there are 3 separate power supplies that generate +/- 5V and +60V voltage required by transmitters circuit. To communicate with the computer there is FTDI USB microchip. All circuits supplied from a single Li-Ion battery cell which can be charged from USB port.

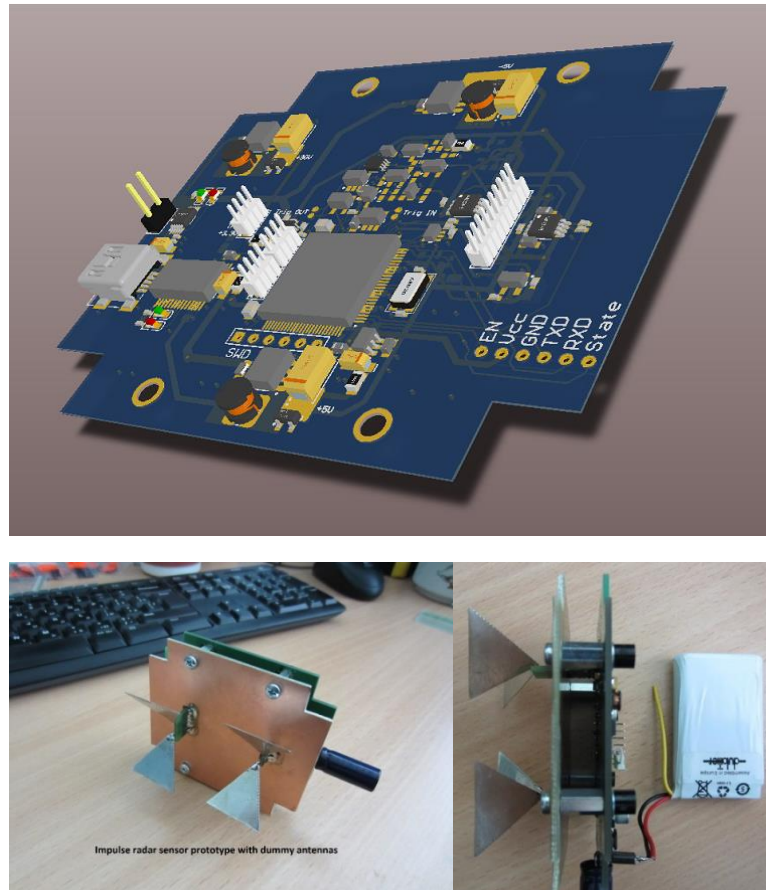


Fig. 3.14. Experimental radar sensor (work in progress).

Besides circuit improvements and debugging a lot of work was done to find suitable antennas for this prototype. Second PCB layer in Fig. 3.14 is used for electromagnetic shielding.



Fig. 3.15. Reflection from an object.

Signal acquired from UWB radar sensor illustrated in

Fig. 3.15. First pulse is not reflected but comes straight form transmitter to receiver by shortest distance, second pulse is reflected from metallic object. There is still necessity to eliminate noisy signal levels and improve transmitted signal that might be tasks for next prototype.

Summary

- Short range UWB radar sensor experimental application tests for security monitoring (work in progress).
- Review on short range UWB radar sensor device standardisation situation in Europe
- Research on methods of improving the UWB radar sensor parameters.
- Research on signal processing methods for detection of changes in a room, object displacement detection.

Development of UWB radar sensor functional parts.

Performance indicators:

1. Scientific publications:

- 1) K. Krumin'sh, V. Peterson, V. Plotsin'sh. The influence of thermal hysteresis of a clocked comparator on the operation of the comparator type sampling converter. Automatic Control and Computer Sciences, July 2015, Volume 49, Issue 4, pp 245-253
- 2) E. Hermanis, M. Greitans, V. Aristov. Identification of characteristics of two-terminal networks from the pulse response of the current. Automatic Control and Computer Sciences, July 2015, Volume 49, Issue 4, pp 239-244.

2. Conference proceedings:

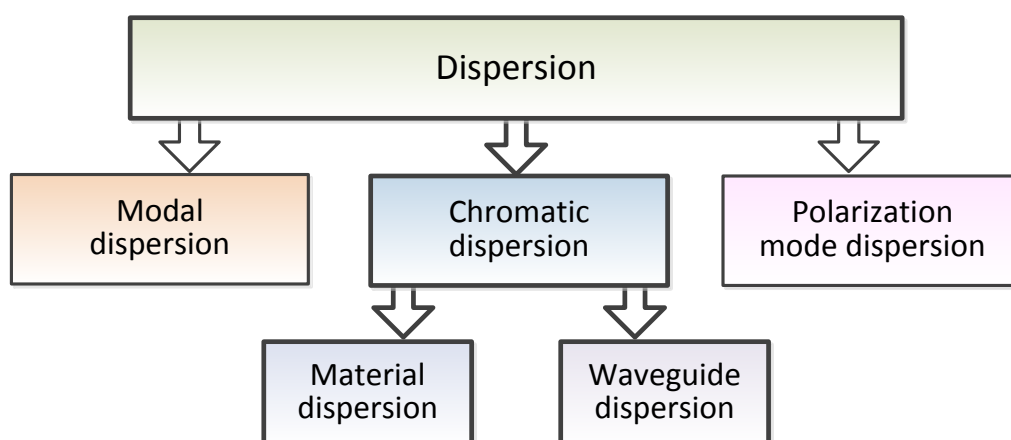
- 1) Aristov, V.; Shavelis, R.; Shupols, G.; Cirulis, R., "An investigation of non-traditional approach to narrowing the GPR pulses," in

Radioelektronika (RADIOELEKTRONIKA), 2015 25th International Conference , vol., no., pp.373-375, 21-22 April 2015.

3. Conference poster:
 - 1) Aristov, V.; Shavelis, R.; Shupols, G.; Cirulis, R., "An investigation of non-traditional approach to narrowing the GPR pulses," in Radioelektronika (RADIOELEKTRONIKA), 2015 25th International Conference.
4. Bachelor thesis:
 - 1) Abajs, M. (2015). Ultra-Wideband Pulse Radar Sensor Application in Security Systems (Unpublished bachelor thesis). Riga Technical University. <https://nda.rtu.lv/en/view/14134>
 - 2) Lielpinka, M. (2015). Remote Sensing Data Acquisition and Processing Using Unmanned Aircraft (Unpublished bachelor thesis). Riga Technical University. <https://nda.rtu.lv/en/view/14023>
 - 3) Maurins, M. (2015). Non-destructive Ice Thickness Monitoring (Unpublished bachelor thesis). Riga Technical University. <https://nda.rtu.lv/en/view/14130>

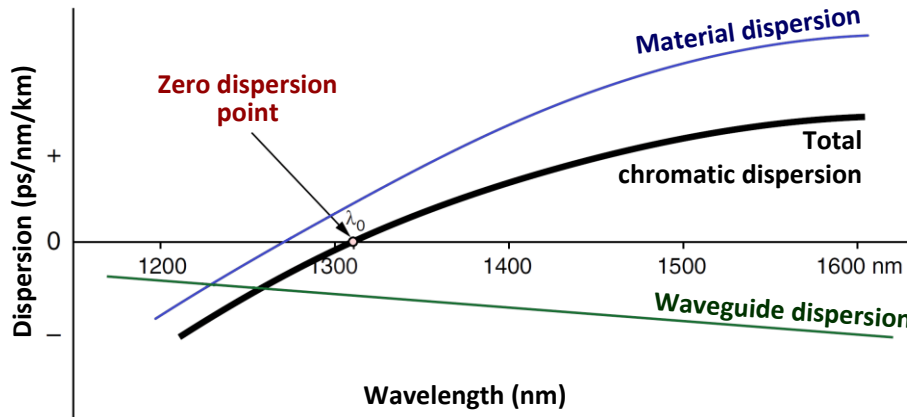
4. RTU TI

In optical transmission systems transmitted optical pulse sequence can be affected by the following dispersion types: modal dispersion, chromatic dispersion, and polarization mode dispersion (see Fig. 4.1). The dominant dispersion types in single mode fiber optical transmission systems are chromatic dispersion and polarization mode dispersion. Modal dispersion can be observed in multimode optical fibers, where multiple modes of the same signal pulse propagate at different velocities along the optical fiber and cause pulse broadening. Generally modal dispersion does not occur in a single mode fiber because there is only one fundamental mode propagating. The reason of polarization mode dispersion is different frequency components of pulse which has different polarization states, resulting in pulse broadening due to different propagation speeds. Polarization mode dispersion becomes a limiting factor for high speed optical communication systems with transmission speed up to 10 Gbit/s per channel.



4.1. att. Dispersion types in single mode fiber optical transmission systems

Chromatic dispersion can be divided into two components - material and waveguide dispersion (see Fig. 4.2). Waveguide dispersion is caused by dependence of propagation velocity for different modes related to the wavelength used for transmission in optical fiber. Waveguide dispersion is affected by physical structure of optical fiber core and cladding (reflective index profile). Waveguide dispersion is relatively smaller if compared with material dispersion.



4.2. att. Chromatic dispersion of standard single mode optical fiber and its components (material and waveguide dispersion)

Waveguide dispersion can be calculated using following equation:

$$D_V = \frac{\lambda \Delta \lambda}{c} 2 n_1^2 \Delta, \quad (4.1)$$

where D_V – waveguide dispersion coefficient, ps/nm/km;

λ – transmitted signal central wavelength, nm;

$\Delta \lambda$ – light source radiation spectral width, nm;

n_1 – optical fiber core light refractive index;

c – speed of light in vacuum, km/s;

Δ – normalized light refractive index difference. $\Delta \approx (n_1 - n_2)/n_2$;

n_2 – optical fiber cladding light refractive index.

Material dispersion is dominant part of chromatic dispersion, and is caused by change of optical fiber refractive index n with wavelength λ used for signal transmission. Material dispersion can be calculated by using the following equation:

$$D_M = \frac{\lambda \Delta \lambda}{c} \frac{d^2 n_1}{d\lambda^2}, \quad (4.2)$$

where D_M – material dispersion coefficient, ps/nm/km;

λ – transmitted signal central wavelength, nm;

$\Delta \lambda$ – light source radiation spectral width, nm;

n_1 – optical fiber core light refractive index;

c – speed of light in vacuum, km/s.

Approximate material (D_M) and waveguide (D_V) dispersion values forming the chromatic dispersion (D_C) value for the standard ITU-T G.652 optical fiber are shown in the table 4.1.

Table 4.1.

Typical values for material, waveguide and total (chromatic) dispersion in a standard single mode fiber at 1310 and 1550 nm wavelengths

Dispersion type	λ , nm	
	1310	1550
D_M , ps/nm/km	2	31
D_V , ps/nm/km	-2	-15
D_C , ps/nm/km	≈ 0	16

For calculation of total chromatic dispersion in standard single mode optical fiber (SSMF) for wavelength range from 1200 nm to 1625 nm the following empirical Sellmeier equation can be used:

$$D_C(\lambda) \approx \frac{S_0}{4} \left(\lambda_c - \frac{\lambda_0^4}{\lambda_c^3} \right), \quad (4.3)$$

here $D_C(\lambda)$ – chromatic dispersion coefficient versus wavelength, ps/(km·nm);

S_0 – zero dispersion slope, ps/(nm²·km);

λ_c – center wavelength of laser emitted radiation, nm;

λ_0 – zero dispersion wavelength, nm.

Zero dispersion slope S_0 is a dispersion parameter that describes the rate of change of dispersion with wavelength at zero dispersion wavelength λ_0 point. Real dispersion representing curve is has a slope and change the value depending on wavelength. It means that at two different wavelengths there will be two various dispersion values.

Zero dispersion wavelength λ_0 is wavelength where optical fiber has its maximum information throughput, because in this point material and waveguide dispersion cancel each other. Typically zero dispersion wavelength of standard SMF optical fiber according to ITU G.652 recommendation is near wavelength of 1310 nm.

Dispersion causes optical signal pulses to broaden and lose their shape as they travel along optical fiber. When pulses become wider, they have tendency to interfere with an adjacent pulses. Eventually this limits the maximum achievable data transmission rate and transmission distance. This broadening of signal pulses causes intersymbol interference (ISI), see Fig. 4.3.

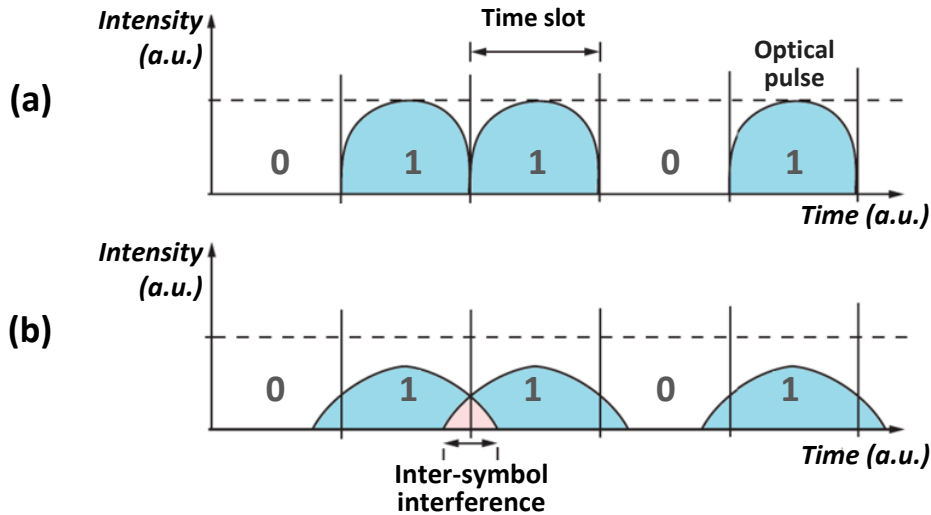


Fig. 4.3. (a) transmitted input bit sequence, and (b) received output bit sequence affected by intersymbol interference (ISI).

As example, if the light source transmits a "1" (light pulse) into an optical fiber then different parts of this pulse will travel along the fiber at different speeds due to dispersion. It means that some parts of the transmitted "1" may spread into the adjacent bit slots.

Therefore, due to influence of intersymbol interference there occur problems to restore transmitted information. In this case it is difficult to separate transmitted bit sequence at receiver side and it is resulting in BER increase and faulty received signal.

In WDM-AON fiber optical access systems dispersion compensation modules (DCM) are used for chromatic dispersion compensation. These modules can provide a fixed or tunable amount of compensating chromatic dispersion (CD) value.

Nowadays, dispersion compensating fiber (DCF) or fiber Bragg grating (FBG) can be used in these chromatic dispersion compensation modules. Typically DCM is specified by what length (in km) of standard ITU-T G.652 single mode fiber will be compensated (usually it is 20 to 80 km) or by the total compensation value of dispersion over a specific wavelength range, specified in ps/nm.

Dispersion compensation module containing dispersion compensating fiber (DCF DCM) typically has a high insertion loss (depending on DCF fiber length it is about 0.5 to 0.6 dB/km). The effective core area (A_{eff}) of a DCF optical fiber is much smaller than standard (ITU-T G.652) single mode fiber, thereby dispersion compensating fiber experience much higher optical signal distortions caused by nonlinear optical effects (NOE): SPM (self-phase modulation), XPM (cross-phase modulation), FWM (four wave mixing).

The effective core area A_{eff} , is optical fiber parameter which determines how tightly light is confined to the core. It is cross-section area of optical fiber along light pulse is propagating. Since the dispersion compensating fiber has small effective core area ($A_{\text{eff}}=20 \mu\text{m}^2$), then light intensity in it is sufficiently high for nonlinear optical effects. This impact of NOE can be reduced by lowering the intensity of optical power.

For example, attenuation coefficient of standard single mode optical fiber typically is $\alpha = 0.2$ dB/km, $A_{\text{eff}}=80 \mu\text{m}^2$. By contrast, dispersion compensating fiber (DCF) has attenuation coefficient of up to $\alpha = 0.6$ dB/km and $A_{\text{eff}}=20 \mu\text{m}^2$.

DCF fiber has large negative dispersion $D = -80$ ps/(nm·km), which helps to compensate accumulated chromatic dispersion in fiber optical transmission line or to do dispersion pre-compensation. Such a negative dispersion coefficient of DCF fiber is obtained during the manufacturing process, by making the complex light refractive index.

Dispersion compensation modules with chirped fiber Bragg grating (FBG) for compensation of chromatic dispersion is also available from manufacturers of optical devices. Chirped fiber Bragg grating is well suitable for WDM-AON systems. It has grating period which is not constant but changes linearly over the length of the grating with the shorter grating period located at the beginning of the grating (see Fig. 4.4). FBG grating period Λ , nm is distance between two adjacent maximum values of the refractive index.

Due to this structure, chirped fiber Bragg grating reflects a narrow spectrum of wavelengths that are centered at λ_B and passes all the other wavelengths, which are traveling in fiber.

Such a grating with a periodically changing structure is produced on silica optical fiber base with germanium impurities in the small fiber core segment, which is irradiated with ultraviolet light. Reflected wavelength λ_B in the fiber Bragg Grating can be obtained by the following equation:

$$\lambda_B = 2\Lambda n_g, \quad (4.4)$$

here λ_B - reflected wavelength, nm;

Λ - grating period, nm;

n_g - fiber's effective group refractive index.

As shown in Fig. 4.4, dispersion affected input pulse with width τ is passing chirped fiber Bragg grating and at output its width is decreased by $\Delta\tau$ and shape is restored. It is achieved because chirped fiber Bragg grating has shorter grating periods at beginning but over the length of the grating these periods linearly increase. Therefore shorter signal wavelengths are reflected sooner and have less propagation delay through the FBG but longer signal wavelengths travel further into the fiber grating before they are reflected back and accordingly have more propagation delay through the FBG.

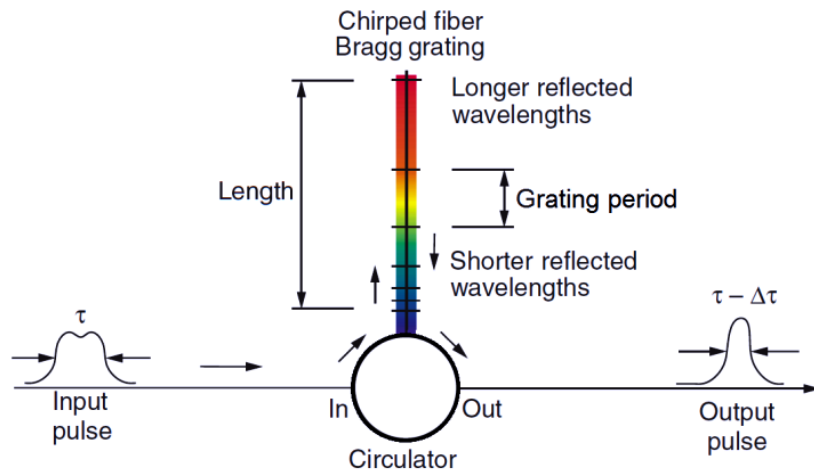


Fig. 4. Example of chromatic dispersion compensation by using chirped Fiber Bragg grating.

Typically, the length of FBG grating is from 10 to 100 cm in commercially available DCM modules. As it can be seen, impact of chirped fiber Bragg grating on optical signal is exactly opposite of optical fiber chromatic dispersion. A significant advantage of using a fiber Bragg grating (FBG) dispersion compensation modules over DCF fiber is its relatively small insertion loss resulting from the insertion of a device in fiber optical transmission system. For comparison, commercial DCF specified to compensate accumulated chromatic dispersion of 100 km standard single mode fiber span have about 10 dB of insertion loss, whereas a FBG based dispersion compensation module (DCM), capable to compensate the same fiber span length, has insertion loss of 3 to 4 dB. In contrast to DCF, FBG based dispersion compensation module can be used at higher optical powers without inducing nonlinear optical effects (NOE) and their influence on transmitted optical signal.

Defended Master thesis:

1. Matīss Viekalis „ Compensation methods of dispersion and research in WDM – PON system”, consultant Prof. Dr.sc.ing. Ģirts Ivanovs;
2. Viktors Romāns „ Research and Evaluation of Chromatic Dispersion Compensation Schemes for Long-Haul Fiber Links”, consultant Prof. Dr.sc.ing. Jurgis Poriņš;
3. Ilona Ābola „ Evaluation of Chromatic Dispersion Compensation Methods in WDM-PON Systems”, consultant Prof. Dr.sc.ing. Ģirts Ivanovs;
4. Alvis Meņģo „ All-Optical Wavelength Conversion in Wavelength Division Multiplexing Systems” consultant Prof. Dr.sc.ing. Ģirts Ivanovs;
5. Agris Sīlis „ Optical Signal Regeneration in Completely Optical Way”, consultant Prof. Dr.sc.ing. Jurgis Poriņš;

Accepted scientific publications:

Spolitis S., Gegere L., Alsevskā A., Trifonovs I., Porins J. and Bobrovs V., Optical WDM - PON Access System With Shared Light Source. Proceedings of Progress in Electromagnetics Research Symposium (PIERS 2015), Prague, Czech Republic, July 6-9, 2015, pp.1–5.

Submitted application for Latvian Patent: “Realization of WDM-PON technology”.

5. RTU BF

Objectives

The first reporting period was mostly related to various organizational, planning, preparative issues. All overall objectives for this starting phase were met; it could be described as successful. The project process went as planned, though some changes and deviations from the proposed plan took place. The main tasks for the first project period were:

1. Perform a literature analysis about the existing methods and technologies used for drinking water on-line monitoring and data analysis and interpretation tools.
Writing a state-of-the-art about on-line drinking water monitoring and early detection systems.
2. Batch experiments. Tests of different methods in batch experiments, which could be used for drinking water network monitoring, and to test the feasibility of the reference biological methods for comparison. Optimization of the methods where it was necessary.
3. Design and installation of the lab-scale experimental pilot system.
4. The first experiments in the pilot system.

Report

5.1.Literature studies

Extensive literature analysis was performed during the first period of the project. More than 67 literature sources, including scientific papers, conference proceedings, book chapters, project reports and industrial offers, were investigated to understand the latest achievements in on-line drinking water monitoring methods, tools and data analysis. The information obtained from these sources was analysed, summarized and presented as a state-of-the-art report. The publication is submitted for the IWA 7th Eastern European Young Water Professionals Conference (Belgrade, Serbia 17 – 19 September) where it will be presented with oral presentation and then included in IWA journal - Water Science and Technology. The title of the article is “Review of Existing and Emerging Biological Contamination Detection Tools for Drinking Water Distribution Systems (DWDS) Online Monitoring”. In short, the methods available for microbial and general contamination events detection have been discussed in relation to possibility of applying them for water quality monitoring in a drinking water distribution system. It appears that although direct sensors might have higher efficiency in detecting specific type of contamination, an approach using surrogate sensors combined with event detection systems (EDS) seems to be more promising for practical application. The principle of event detection system operation has been reviewed in detail. It was concluded that, however, choice of water quality parameters used for analysis by an event detection software as well as adjustment and configuration of event detection software is critical and more research including case studies is needed to find the set of parameters that help to maximize event detection efficiency without unnecessary increase of monitoring station costs. The article contains the following sections at the current state: Surrogate sensors (non-compound sensors), Selection of parameters, Commercially available sensors, Biological

methods and sensors for online drinking water quality monitoring, Data analysis, Event Detection Systems, Application of neural networks for data analysis.

1. Batch scale experiments

The batch tests were conducted to check availability, reproducibility and feasibility of some of the tools and methods, which could be used manually and/or developed as on-line tools. It was planned to test flow cytometry methods, ATP measurements, chlorine in-situ approach, total organic carbon (TOC) measurements and microorganism growth potential.

Chlorine and TOC measurements are chemical water quality parameters, and are often used as sensors in chlorinated drinking water. In our case it is still an issue whether these methods will be measured on-line or will be detected manually. The reason for these doubts is that drinking water in Latvia is not always chlorinated, or residual chlorine dose is so low (e.g. the measurement in Riga showed only 0.03 mg/L of free chlorine in the effluent of the treatment plant), that it is not feasible to build the sensor and monitor it continuously. That is why it was decided to use chlorine measurements mostly as the additional parameter rather than one of the main water quality indicators. The measurements of free and total chlorine were tested in the lab with Hach DPD free and total chlorine reagent powder pillow and measured with Hach DR-890 prior the experiments. Standard deviation of the method was 0.01 mg/L for total chlorine, and 0.025 mg/L for free chlorine measurements.

As for TOC, this parameter might be important for water quality monitoring. The existing method for TOC determination is based on total carbon (TC) and inorganic carbon (IC) measurements on Skalar Formacs^{HT} analyser. The measurements were performed with autosampler, and the standard deviation of the measurements ranged from 0.11 to 1.74 % for TC and from 0.04 to 0.76 % for IC. Although the errors are quite low, development of another, non-purgeable organic carbon (NPOC) based determination method, is considered. The reason for that (SLMB, 2012) is that these results were obtained from the samples with relatively high TOC (more than 3 mg/L). For concentrations less than 1 mg/L, the method could give higher standard deviation, especially if considerable fraction of the carbon is inorganic. 1 mg/L of TOC is very probable concentration for drinking waters.

Adenosine-triphosphate (ATP), flow cytometry and growth potential tests are meant to describe water biological quality. Due to technical reasons it was not possible to make ATP tests during the first period of the project. Based on the previous experience, the method is very precise and accurate, and it would be very interesting and challenging to use it as a sensor to describe water quality.

Flow cytometry (FCM) measurements were performed on Partec CyFlow instrument, and two basic methods were tested – determination of total cell count and intact cell count. For total cell count SYBR Green I (SG) stain was used for labelling the cells. The applied method was adopted from the one standardized by other researchers (SLMB, 2012)⁹. Intact cell count was determined with SG and propidium iodide (PI)

⁹ SLMB, 2012. "Method 333.1: determining the total cell count and ratios of high and low nucleic acid content cells in freshwater using flow cytometry." of high and low nucleic acid content cells in freshwater using flow cytometry," in *Schweizerisches Lebensmittelhandbuch* (Bern: Federal Office for Public Health).

stain (SGPI). In contrast to SG staining method, SGPI has not been standardized up to our knowledge, and the method, used for this study, was optimized from the methods described in various sources (Berney et al., 2007¹⁰; Hammes et al., 2010¹¹; Van Nevel et al., 2013¹²). In our case feasibility and necessity of EDTA was tested, what is very important issue both for SG and SGPI staining. Additionally DMSO and Tris buffer were tested as the stain solvents. The first testing results are shown on Fig. 5.1.

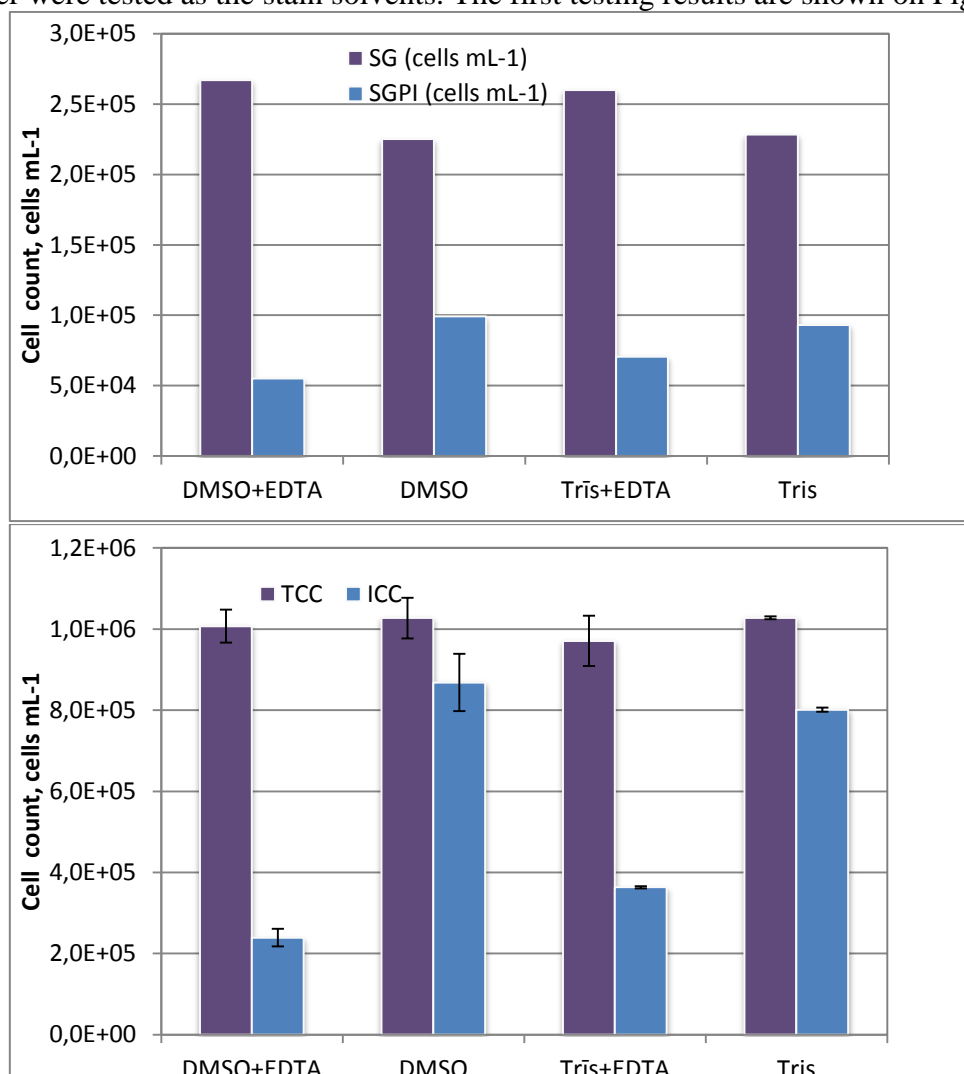


Fig. 5.1. Intact and total cell counts obtained with SGPI and SG stains, respectively. The water samples used in this study were untreated river water (A), and chlorinated tap water (B). Measurements were performed on Partec CyFlow in triplicates.

The main conclusion from these experiments are: (i) less ICC with EDTA in all samples; (ii) difference in ICC is higher in non-chlorinated samples, which might be

¹⁰ Berney, M., Hammes, F., Bosshard, F., Weilenmann, H.-U., Egli, T., 2007. Assessment and interpretation of bacterial viability by using the LIVE/DEAD BacLight Kit in combination with flow cytometry. *Appl. Environ. Microbiol.* 73, 3283–3290. doi:10.1128/AEM.02750-06

¹¹ Hammes, F., Goldschmidt, F., Vital, M., Wang, Y., Egli, T., 2010. Measurement and interpretation of microbial adenosine triphosphate (ATP) in aquatic environments. *Water Res.* 44, 3915–3923. doi:10.1016/j.watres.2010.04.015

¹² Van Nevel, S., Koetzsch, S., Weilenmann, H.-U., Boon, N., Hammes, F., 2013. Routine bacterial analysis with automated flow cytometry. *J. Microbiol. Methods* 94, 73–76. doi:10.1016/j.mimet.2013.05.007

explained that EDTA provides better staining (CI samples are already permeable enough for PI); (iii) EDTA provides better SG staining in chlorinated water; (iv) no real difference between DMSO/noDMSO samples. However, these results rise other questions, e.g. if it works for all natural and chlorinated waters. 9 different water sources were chosen to investigate this question, which included different types of tap water, natural bottled water, river water, public water pump and sea water (Figure 5.2). The observations are similar to the experiment before – less intact cells with addition of EDTA, but in the present experiment (Figure 2) less TCC was observed. However this data set also showed some interesting aspects of interaction between EDTA and water bacteria. One of the conclusions is that the more sample is diluted, the less TCC and ICC is detected, which could be explained by stain leakage out of the cell or disruption of the cell wall as a result of osmotic pressure caused by following dilution.

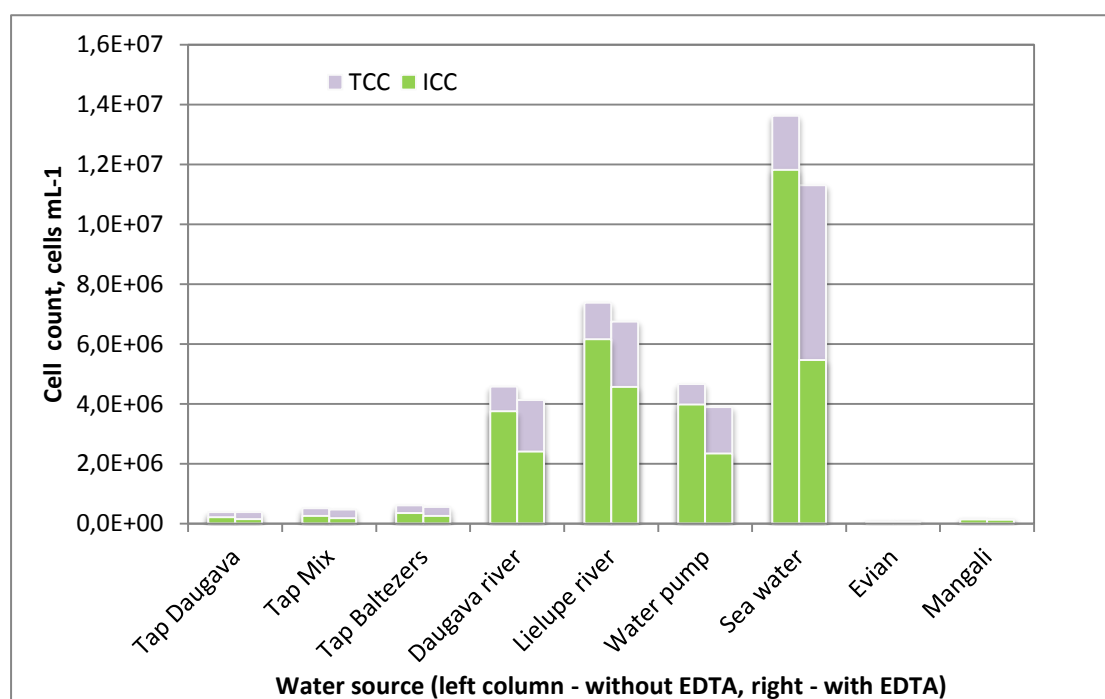


Fig. 5.2. Intact and total cell counts obtained with SGPI and SG stains, with and without EDTA. Measurements were performed on Partec CyFlow in triplicates.

Based on the data obtained, it was decided to continue determination of ICC and TCC in drinking water samples without using EDTA while staining. These results will complement the upcoming publication with the working title “Optimization of SGPI staining method for drinking water quality characterization”.

Microorganism growth potential is a biological stability indicator, meaning that this is a parameter, which can describe water quality considering its chemical and physical properties to support bacterial growth. Although, it cannot be used for on-line monitoring, this might be very useful additional reference parameter for field data interpretation and analysis. Several control test were performed to test the reagents and test conditions, and it was concluded that direct incubation has to be applied for growth potential tests. Quenching with 0.5 mM NaNO₂ has to be applied and

inoculum added for chlorinated water samples. Additionally, different nutrient limitation could be tested.

As a conclusion, ATP and FCM will be the main biological methods used for the further activities, evaluation of biological stability should be considered for simulation experiments and later might be used for as online or semi-online sensors. Chlorine measurements will be performed in-situ if feasible, and necessity of TOC sensor will be tested further. As for other physically-chemical parameters for on-line monitoring Total organic carbon (TOC), electrical conductivity (EC), pH, temperature, Cl ions, oxidation – reduction potential (ORP) were chosen.

5.2. Design of the lab-scale experimental pilot system.

Based on the literature studies and batch experiments, the lab-scale experimental pilot system was designed. The aim of the system is to reach hydraulic, biochemical and physical conditions that might exist in real DWDS and transfer batch scale experiments in an environment that is more similar to natural conditions in DWDS. The system was designed to meet maximum available size of it and laboratory dimensions (Figure 5.3). The system is equipped with online sampling points where online sensors for Temperature, pH, Electrical conductivity, Cl ions, Oxidation-reductions potential, Total organic carbon measurements might be done. The sensors installed in the system are *Hanna Instruments Inc.* production. All of the data collected from the online sampling points are sent to the computer where it might be analysed. Also electromagnetic flow meter and manometers are installed to monitor the hydraulic parameters of system. In future the hydraulic parameters are going to be automated.



Fig.5.3. Pilot scale DWDS.

Pilot system parameters:

- pipe length – 200 meters (for experimental usage) + 100 meters for supply and waste water;
- pipe diameter – 25 mm (inner), 33 mm (outer);
- pipe material – PVC (polyvinylchloride);
- water source – Riga city DWDS;
- dosage points – 1;

- manual sampling points – 3;
- sampling points equipped with online sensors – 2;
- max designed pressure – 1 bar;
- average designed flow velocity – 0.1 m/s;
- average designed hydraulic retention time – 30 minutes;
- total volume of experimental piping – 98,17 litres;

5.3. First experiments with the pilot system.

In terms of experiments in pilot scale system there were numerous experiments done to adjust the sensors and data collection system. No experiments related to scientific part and methods of the project have been done. Experiments with bacterial contamination and event detection are going to be carried out during the 2nd and 3rd year of the research.